


Article

On the Applicability of Laboratory Thermal Infrared Emissivity Spectra for Deconvolving Satellite Data of Opaque Volcanic Ash Plumes

Daniel B. Williams * and Michael S. Ramsey 

Department of Geology and Environmental Science, University of Pittsburgh, 4107 O'Hara Street, Pittsburgh, PA 15260, USA; mramsey@pitt.edu

* Correspondence: dbwilliams@pitt.edu; Tel.: +1-412-628-8784

Received: 30 August 2019; Accepted: 1 October 2019; Published: 5 October 2019



Abstract: The ASTER Volcanic Ash Library (AVAL) is presented, developed using quantitative laboratory thermal infrared (TIR) emission spectroscopic methods, spanning the 2000–400 cm^{-1} (5–25 μm wavelength) range, including the Earth's TIR atmospheric window (8–12 μm). Each spectral suite is unique owing to the chemical composition and proportion of glass to crystals per sample and is divided into six size fractions. AVAL, used with an appropriate spectral mixture model applied to orbital multispectral TIR data, provides a unique ability to study active volcanic ash plumes. We present the first example of this application to an ash plume produced by the Sakurajima Volcano in Japan. The emissivity variations measured in ash plumes using an ever-expanding ash spectral library will provide future quantitative inputs for both atmospheric models, where the ash composition is unknown or estimated, as well as compositional probes into ongoing eruptions.

Keywords: volcano; ash; TIR; emissivity; spectroscopy; ASTER

1. Introduction

Explosive volcanic eruptions produce plumes of ash, a complex mixture of glass, lithic and mineral fragments [1], ranging in size from <2 mm to sub-micron [2]. These plumes are formed by decompression fragmentation of the parent magma, with higher degrees of fragmentation associated with higher viscosity magmas [3,4]. Ash is commonly divided into two classifications based on particle size; particles <63 μm are considered fine ash, whereas coarse ash, is particles 0.063 to 2 mm [5]. Coarse particles (and aggregates of finer particles) tend to fall out of suspension first, depositing close to the volcano [6–10]. Finer particles, however, can travel greater distances in concentrations easily detected by orbital sensors.

Ash is one of the most spatially wide-ranging volcanic hazards to life and property [11]. It is an irritant for human beings and animals, capable of causing respiratory problems [12,13]. Furthermore, sufficient quantities of ash fall can damage infrastructure, affecting the structural integrity of buildings [14], communication and electrical power lines [15], and agricultural systems [16]. Additionally, there are widely documented issues regarding aircraft safety [17]. Ash will abrade windows and wing tips, damage the ventilation systems, and if ingested into the engines, result in re-melting and subsequent cooling onto the turbine blades, potentially causing engine failure.

Ash analysis is essential in characterizing the eruptive state of a volcano and its potential for future activity [18]. Many volcanoes, however, are in remote regions and direct observations of their regular activity is impractical [19]. With improvements in the spatial, spectral and/or temporal resolution of satellite sensors, their data is becoming an increasingly vital tool in the characterization of volcanic activity. Thermal Infrared (TIR) remote sensing of volcanic ash commonly focuses on the

initial detection of the drifting ash cloud with high temporal, low spatial resolution satellite sensors, that include, but are not restricted to, the Moderate Resolution Imaging Spectroradiometer (MODIS), the Atmospheric Infrared Sounder (AIRS), Spin Enhanced Visible and Infrared Imager (SEVIRI) and the Imager instrument on the Geostationary Operational Environmental Satellite (GOES), to aid in aircraft hazard mitigation [20]. These data are coupled with computer models to forecast future paths of the ash cloud as it travels away from its source [21]. High spatial resolution satellite sensors are not routinely used to detect volcanic ash plumes, although Advanced Spaceborne Thermal Emission and Reflection Radiometer (ASTER) TIR data has been shown to be sensitive to volcanic SO₂ [22,23], ASTER has not been used to analyze the ash content of volcanic plumes.

Detection of ash in the TIR relies on the interaction of upwelling radiance from the ground/ocean surface through portions of the plume that are TIR-transparent, referred to as the “split-window” or “Brightness Temperature Difference (BTD)” technique [24–29]. Ash clouds are distinguished from meteorological clouds through the apparent temperature difference resulting from the change in transmission spectrum between channels centered at 11 and 12 μm. This interaction between upwelling ground radiance and ash particles can provide the particle-size distribution (PSD), mass loading, effective particle radius, the Aerosol Optical Depth (AOD) and the plume top altitude [30,31]. Ash composition and particles >15 μm are not directly measured using these techniques, however [32–34]. Furthermore, these techniques are reliant on an assumption of the optical properties of the material, using these properties to retrieve information in the cloud [35,36]. However, these assumptions can lead to inaccurate TIR retrievals [37], and so determining the composition of the erupted material is an important input to these models. The potential exists to use emission spectroscopy as a method to determine this.

TIR data can be acquired using remote sensing data, as well as laboratory spectroscopy methods, allowing for the direct application of laboratory data to image analysis. Furthermore, a TIR emissivity spectrum produced from multiple mixed components has long been shown to be the linear spectral sum of the areal percentage from each of those components [38]. This allows for a relatively straightforward approach to deconvolving these spectra using appropriate end-member libraries, making compositional determination possible. Emission spectroscopy is a non-destructive analysis that can be used to assess both the composition and particle size of a geologic material [38–40]. Compiling laboratory spectral data into various libraries allows for the subsequent analysis of unknown materials. Spectral libraries exist for both reflectance [41,42] and emission [43] analysis. These are, primarily, pure mineral suites, some of which collected measurements of different particle-size fractions, and are suitable for mapping ground surfaces and rock, not airborne ash.

Volcanic ash clouds and ash-fall deposits contain both very fine particles, and a significant silicate glass component (~ 20–80 wt. %, [44]). The glass generated from the eruption may also differ in SiO₂ content relative to that of the bulk composition of the magma, as crystallization of the magma leaves behind a melt of more evolved composition from which this glass is derived [45]. The spectral features of a given glass composition are broader than that of its crystalline counterpart and are muted or lacking entirely in the glass phase [46]. This is caused by the marked changes in the atomic bond structure and vibrations produced during depolymerization of the crystal structure [47]. Volcanic glasses have been previously analyzed through TIR spectroscopic methods [46–48], although these libraries are restricted to one particle size, which makes them unsuitable for volcanic ash studies, given the need for spectra representing several particle-size ranges, and that volcanic ash samples are material mixtures. Therefore, a laboratory-measured spectral library of natural volcanic ash samples is required.

In this paper, we present laboratory-derived TIR emission spectra of volcanic ash samples at well-defined particle-size ranges, dubbed the ASTER Volcanic Ash Library (AVAL), and the first application of this data suite to a volcanic ash plume captured by the ASTER TIR system. We describe the laboratory techniques used to create this library, the effects of sample petrology on the TIR emission spectra, and the success of their application to orbital data.

2. Materials and Methods

2.1. Sample Collection

Volcanic ash samples were acquired from selected volcanic centers (Table 1), chosen because the material was available shortly after deposition (seconds to days) and, therefore, were likely to be free of weathering products. As more samples are collected and processed, they will be added to the library to increase the compositional diversity. This library is complemented by a crushed and powdered obsidian, obtained from the Mono-Inyo domes complex, California. This sample, while not collected recently after the eruption as the other samples, serves as the high-silica pure glass end-member, as it is a naturally occurring volcanic glass. This sample was crushed by hand using an agate mortar and pestle to produce the appropriate particle sizes for use in the spectral analysis.

Table 1. Samples currently available in the volcanic ash spectral library.

Volcano Name (Country)	Collected/Donated	Date of Collection	Eruption Style	Coordinates (UTM)/Notes
Fuego (Guatemala)	Collected	02/24/2015	Strombolian	Trinidad Barranca, Volcán De Fuego, Guatemala (15P, 729744.46m E, 1597125.24m N)
Sakurajima (Japan)	Donated	07/22/2013	Vulcanian	Collected during active ash fall. Sakurajima, Japan (52R, 659328.42 m E, 3492357.64 m N)
Santiaguito (Guatemala)	Collected	03/07/2016	Vulcanian	Opposite 2007 lava flow, Santiaguito, Guatemala (15P, 653738.00m E, 1626906.00m N)
Soufrière Hills Volcano (SHV) (Montserrat)	Donated	02/2010	Vulcanian	Belham Valley, Montserrat †
Mono-Inyo Craters (USA)	Collected	07/15/2012	Sub-Plinian	Mono-Inyo Craters complex, California, USA. Sample is glassy obsidian that was crushed and sieved (11S, 321901.22 m E, 4180047.07 m N).

† Specific sample coordinates and collection date are not known.

2.2. Sample Preparation and Separation

Samples are dried at 80 °C for 12 hours, and then separated by dry sieving into >150, 63–150, 45–63 and <45 µm size fractions. The >150 µm fraction is washed with acetone to remove any smaller clinging fine-grained particles that can reduce the spectral contrast due to surface scattering [49]. Ramsey and Christensen [38] demonstrated that non-linear spectral mixing dominates below 63 µm. They also showed, however, that linear unmixing analysis of these size fractions remains viable provided the corresponding particle-size spectral suite is used. For the <45 µm size fraction, a different separation method is needed. A Microorifice Uniform Deposit Impactor (MOUDI) [50] is used to separate this ash into three additional size fractions based upon their aerodynamic radius: 25–45 µm, 8–25 µm and <8 µm. This is located at the Air Quality Laboratory, Carnegie Mellon University, Pittsburgh PA. This is a type of inertial impactor which draws air in to the apparatus (Figure 1) through a regulated tap and drawn through to the other side by a pump. Particle-size ranges are calculated using the Stokes number (St):

$$St = \frac{\rho_P C V_o D_P^2}{9\mu W} \quad (1)$$

where ρ_P is the particle density, C is the slip correction, V_o is the average air velocity at the nozzle exit, D_P is the particle diameter, μ is the air viscosity and W is the nozzle diameter. This equation helps to predict whether a particle will remain suspended and continue to travel through the MOUDI, hitting the impaction plate. The flow rate is adjustable so that the specific particle-size range collected at each stage can be determined.

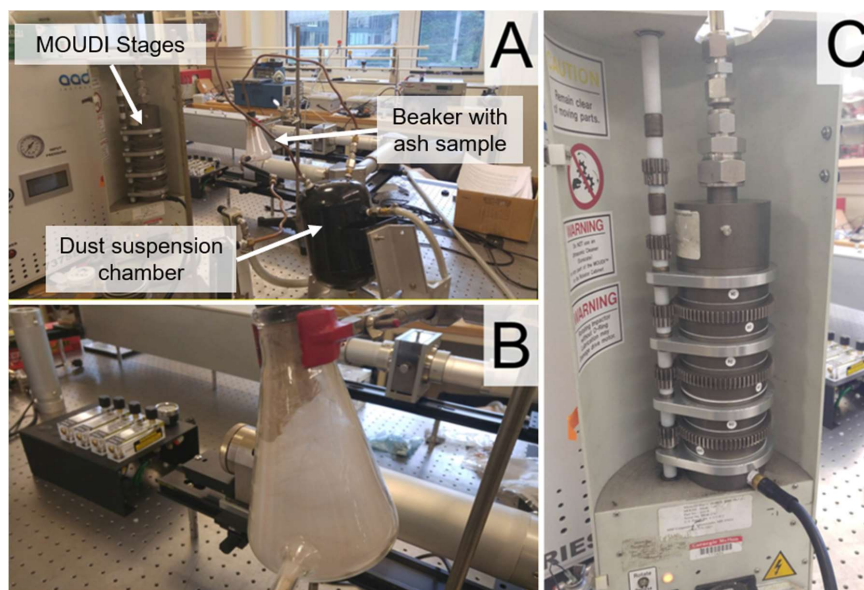


Figure 1. The MOUDI instrument at the Air Quality Laboratory, Carnegie Mellon University. (A) Laboratory set-up where air is regulated to the appropriate flow rate before entering the beaker; (B) beaker containing the ash sample, which is drawn into the dust suspension chamber before entering the MOUDI stages; (C) different particle-size stages. A pump is attached to the base of the final stage and used to draw the air and suspended particles through each MOUDI stage.

A flow rate of 15 L/min is used for the separation, which allows the ash particles to be subdivided into the three size fractions. The sample is placed within a chamber and compressed air introduced, creating a particle suspension that is transported into a dust suspension chamber. A second air pump is used to draw air out of the dust suspension chamber and into the MOUDI system. A series of aluminum foil impaction plates are set on top of each MOUDI stage. These stages rotate to allow uniform deposition of particles across the substrate once the ash enters the MOUDI inlet. Depending on the aerodynamic radius of the particle and the cut point size (i.e., the size and shape of the holes on the MOUDI stage), finer particles will remain suspended, whereas larger particles will impact onto the substrate. This was performed several times for durations of 15–20 min. Each sample was collected by mixing it with acetone to remove it from the substrate.

2.3. Collection of Emissivity Spectra

Emissivity spectra are acquired at the University of Pittsburgh infrared spectroscopy laboratory. The methodology used here relies on the energy from the heated sample as the source. The calibration procedure is described by Ruff et al. [51] using the following equation;

$$\epsilon_{\text{samp}} = \frac{\frac{V_{\text{meas}}}{F} - B_{\text{env}} + B_{\text{inst}}}{B_{\text{samp}} - B_{\text{env}}} \quad (2)$$

where ϵ_{samp} is the emissivity of the sample, V_{meas} and F are the measured voltage and calculated instrument response of the spectrometer, respectively. The other emitted energy terms are the environmental (B_{env}), the instrument (B_{inst}), and the sample (B_{samp}) energies. F is calculated using two blackbody measurements. These are custom made 45° cone blackbodies coated with a high-emissivity paint, which closely approximates a perfect blackbody.

Samples are placed in 2.5 cm-diameter copper cups and left in a drying oven at 80 °C for 24 h. Heating the sample above background/room temperature improves the signal to noise ratio of the data [43]. To avoid a preferential grain orientation, samples are not levelled or compressed. Each spectrum is acquired using a Nicolet Nexus 670 FTIR Spectrometer. The spectrometer uses a XT-KBr beamsplitter

and a mercury cadmium telluride (MCT-B) detector cooled with liquid nitrogen (LN₂). A glovebox adjacent to the spectrometer contains the sample measuring apparatus. The glovebox/spectrometer temperature and humidity are precisely monitored, resulting in high-precision emissivity spectra. Both the spectrometer and the attached glovebox are purged with dry air to limit spectral obscuration by H₂O and CO₂. Each sample is removed from the oven and placed onto a heated stage, kept at the same temperature as the oven, within the glovebox and left until it thermally equilibrates. It is raised up into a thermally controlled chamber maintained at 25 °C and the emitted sample radiance is directed into the spectrometer by way of a collimating mirror located above the chamber. A total of 512 individual scans of the sample are acquired and averaged, with a spectral sampling of 4 cm⁻¹. These data are converted to calibrated emissivity using Equation (2). This configuration captures data that are directly comparable to those obtained from satellite sensors following their correction for the intervening atmosphere. The laboratory-resolution emissivity spectra are then analyzed and subsequently resampled to the five-point ASTER TIR spectral resolution using the pre-defined ASTER filter function.

The estimated measurement error was determined by calculating the noise equivalent delta emissivity (NEΔε) of the spectrometer. Measured radiance from the 100 °C laboratory blackbody was subtracted from that of a calculated (theoretical) blackbody emitter. The overall NEΔε across the 2000–400 cm⁻¹ wavenumber range is 0.83%, with a standard deviation of 0.74%. Significant to this study is the uncertainty over the ASTER TIR region (~1250–833 cm⁻¹, 8–12 μm). Here, the NEΔε improves (0.46% with a standard deviation of 0.01%). The NEΔε at each ASTER spectral band position is added to the AVAL spectra presented in Section 3 as an indicator of measurement uncertainty and measurement repeatability.

2.4. Additional Analyses

A polarized light microscopy examination of 2.5 g of each volcanic ash sample was performed by RJ Lee group (Monroeville, PA) to determine the % glass to crystal content (Table 2). Additionally, an X-Ray Fluorescence (XRF) analysis of 2 g of each ash sample was performed at Franklin and Marshall College by Stan Mertzman using a Malvern PANalytical Inc. Zetium X-Ray Fluorescence vacuum spectrometer. Samples are placed in a muffle furnace at 950 °C for 1.5 h. Upon removal, these are cooled in a desiccator at room temperature, and re-weighed to obtain the total volatile content (% LOI). Then, ~0.4 g of the anhydrous powder is mixed with 3.6 g of lithium tetraborate. This mixture is placed in a platinum crucible and heated over a meeker burner until molten. This is mixed further while still molten, and then quenched in a platinum casting dish to produce a glass disk used for analysis. A working curve is calculated for each element by analyzing known geochemical standards [52,53].

3. Laboratory Results

The first additions to AVAL are shown in Table 1. The library currently contains 30 individual spectra. These data will be available from the Image Visualizations and Infrared Spectroscopy (IVIS) research group archive (<http://ivis.eps.pitt.edu/archives/>) at the University of Pittsburgh. As additional spectra are added to the library, this will be noted in the accompanying data. We present these at both laboratory hyperspectral and ASTER TIR multispectral resolution. All the samples have a reststrahlen band feature between 1250 and 800 cm⁻¹ (8–12.5 μm), the exact width and position of which is the most diagnostic of composition [39,43]. The results from the optical and TIR spectral analyses show that the dominant phase is volcanic glass in all cases except that of Fuego, which contains only 20% glass, and appears to be dominated by a plagioclase feldspar spectral feature, when compared with pure mineral spectra of feldspar minerals found in the Arizona State University Spectral Library [43]. The other ash samples ranged from 64–76 wt. % glass (Table 2). Where glass is the dominant component, the spectral features of the minerals are reduced in proportion to their lower abundance. However, mineral components are still present, with plagioclase feldspar assumed to be responsible for several spectral features seen in the ~1200–800 cm⁻¹ (8.3–12.5 μm) and ~650–500 cm⁻¹ (15.4–20 μm) ranges.

Additionally, the SHV spectrum would appear to contain a silica polymorph component, as seen in the $\sim 1215\text{--}1050\text{ cm}^{-1}$ ($8.2\text{--}9.5\text{ }\mu\text{m}$) range, when compared to spectra of crystalline silica minerals [43].

Table 2. Basic spectral and compositional information of the AVAL samples.

	Fuego	Sakurajima	Santiagouito	SHV	Mono-Inyo Obsidian
Christiansen Frequency (cm^{-1}/λ)	1265/7.9	1290/7.8	1305/7.7	1338/7.4	1322/7.6
ϵ minimum (cm^{-1}/λ)	1001/9.9	1086/9.2	1090/9.2	1093/9.1	1084/9.2
Measured Glass/Crystals (%)	20/80	64/38	64/38	76/24	100/0
Wt. % SiO_2	53.82	58.46	60.16	62.67	73.92

The positional change of the Christiansen frequency emissivity maximum to shorter wavelengths is attributed to an increase in SiO_2 in the sample [54]. This increase is seen in Figure 2, where the emissivity maximum shifts from 1265 cm^{-1} ($7.9\text{ }\mu\text{m}$) for Fuego to 1338 cm^{-1} for SHV ($7.4\text{ }\mu\text{m}$). A discrepancy exists for the Christiansen frequency of the SHV sample relative to the Mono-Inyo obsidian. This may be because of the crystalline polymorph, which would cause a shorter wavelength Christiansen frequency position, despite SHV having an average lower SiO_2 content.

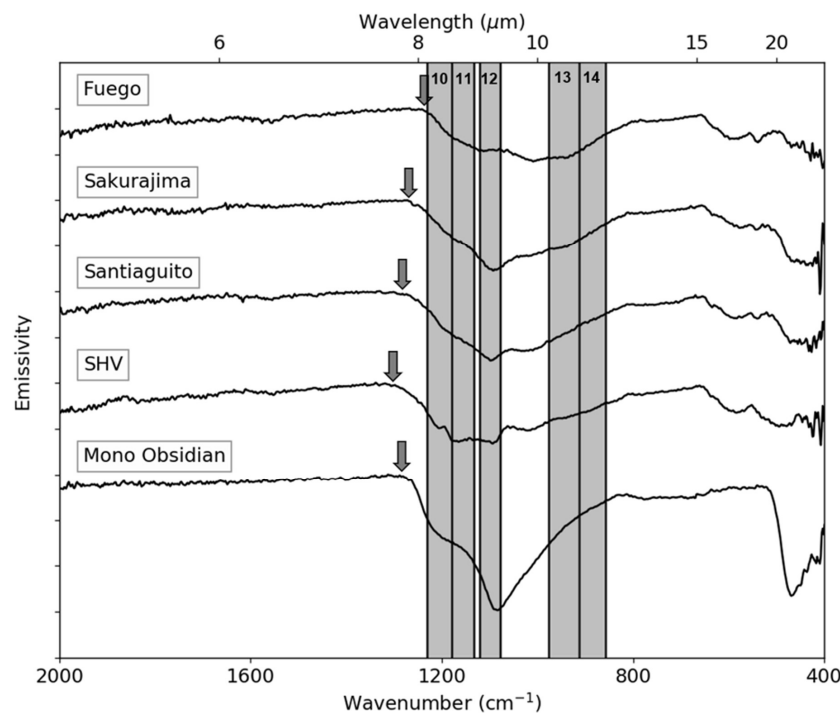


Figure 2. AVAL emissivity spectra of the largest particle-size fraction of each library sample (offset for clarity). Each tick on the y-axis represents an emissivity of 0.05. ASTER TIR bands/band widths are shown with their corresponding band number. Arrows show the location of the CF for each spectrum (where $\epsilon = 1$).

The full laboratory and ASTER resampled resolutions of all the ash samples are shown in Figure 2, subset to the ASTER TIR spectral range of $1250\text{ to }833\text{ cm}^{-1}$ ($8\text{--}12\text{ }\mu\text{m}$). The shift to higher wavenumber (lower wavelength), resulting from increasing SiO_2 content is seen in the AVAL spectra as a lower emissivity at shorter wavelengths (e.g., ASTER band 10; $8.291\text{ }\mu\text{m}$) for the more silicic samples. Figure 3 also demonstrates the level of success obtained by the sample cleaning, sieving and MOUDI separation for each size fraction, which eliminates the introduction of contamination possible in other separation approaches. In most cases, each spectrum is distinct (non-overlapping) with smaller particle-size fraction spectra having progressively higher overall emissivity caused by increasing particle scattering created by the larger surface area of smaller particles, thus a greater amount of

energy is detected [34]. This increase in emissivity for the primary spectral feature is coupled with the development of transparency features (TF) at lower wavenumbers, the depth of which conversely increases as particle-size decreases, caused by volume transmission in this wavenumber region [55]. In the AVAL spectra, the development of this TF is visible as a reduction in emissivity at $<900\text{ cm}^{-1}$ ($<11.1\text{ }\mu\text{m}$). Only the Fuego spectra display less distinction between certain particle-size fractions, which is particularly evident in the two largest. This may be caused by the higher mineral percentage in this sample or potentially the presence of small vesicles, which mimic the behavior of a blackbody and decrease the spectral contrast [56]. The combination of spectral shape, band depth and the appearance of lower wavenumber transparency features demonstrates, however, the unique nature of each spectral suite, and their potential application for deriving both composition and particle size from emissivity data extracted from TIR image data of an active plume.

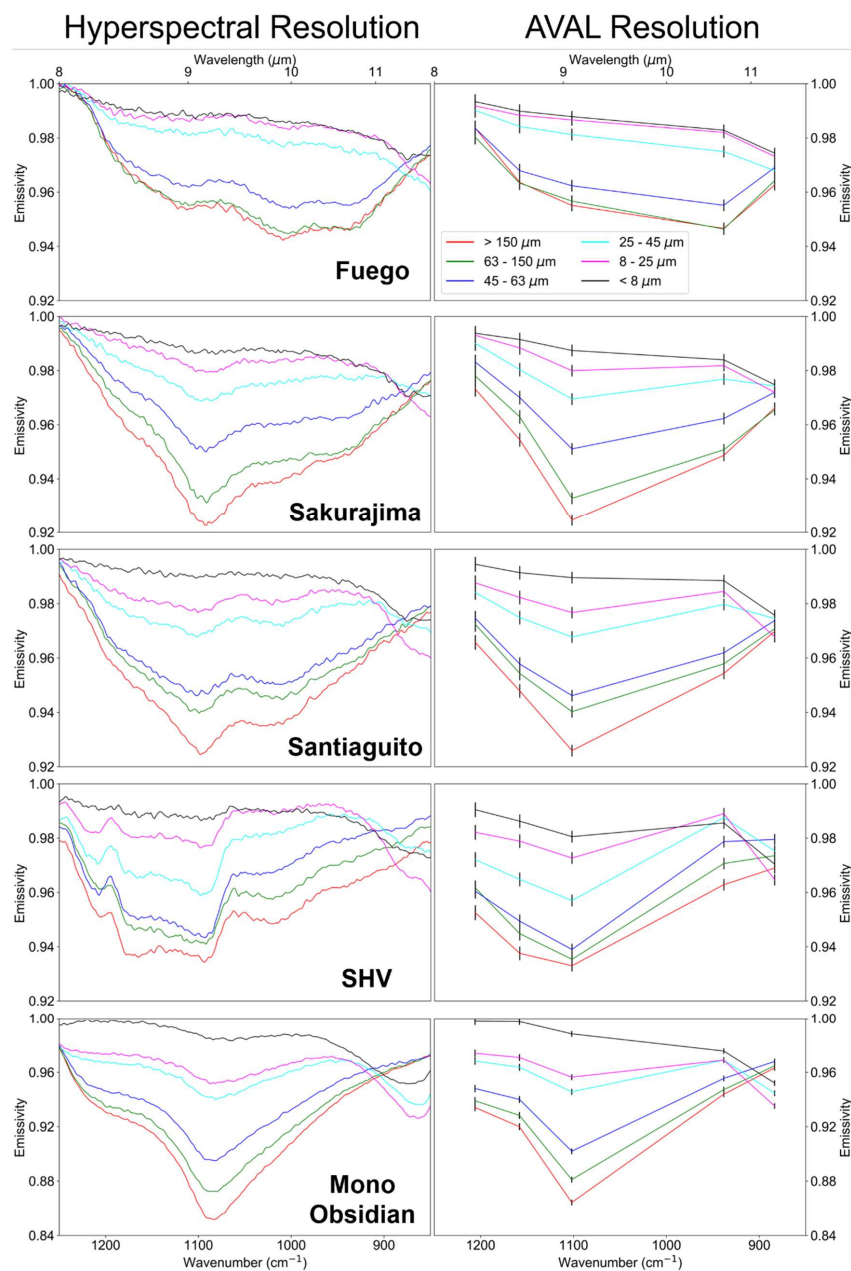


Figure 3. Laboratory spectra of the entire suite subsampled to the ASTER spectral range. Spectra are shown at the full laboratory hyperspectral and the five-point AVAL resolution. Estimated measurement uncertainty is shown as vertical bars on the AVAL spectra.

The XRF analysis further provided the opportunity to determine the geochemical “uniqueness” of each sample. The eventual aim of AVAL is to encompass the whole range of lithologies that exist, in order to better determine the composition of erupted material that is captured by TIR image data. The current range of compositions available in AVAL is shown in Figure 4. While at this early stage, the library is by no means complete, each of the current samples is geochemically different enough to warrant a place in the library. As more samples become available, we hope to increase the lithologies represented.

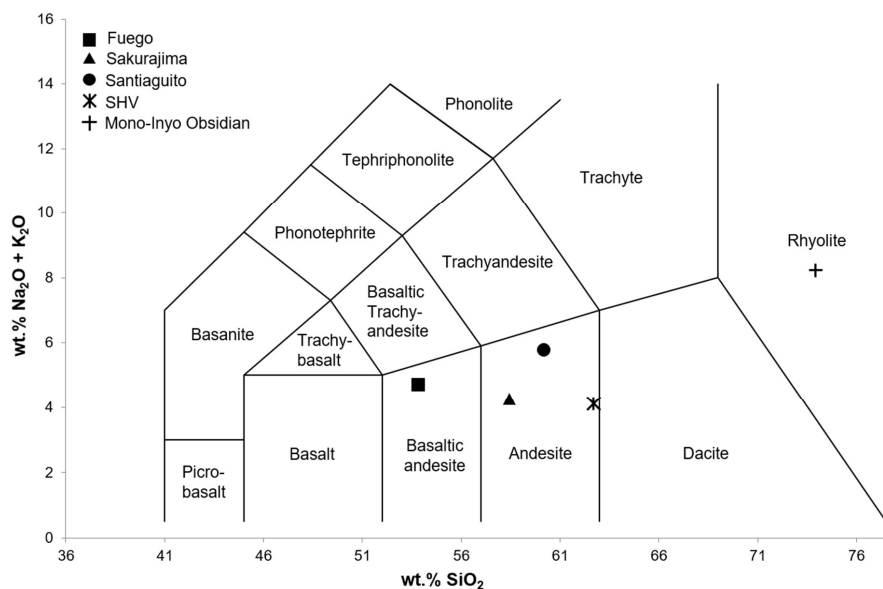


Figure 4. Total Alkali Silica (TAS) plot for the five initial members of the AVAL spectral suite. Whereas there are clear chemical distinctions between each of the currently selected end-members, there are several different compositions that still need to be added to the library.

4. Application to ASTER Data

The primary goal for developing this spectral library was to obtain quantitative compositional and particle-size information of volcanic ash plumes captured by ASTER. ASTER is not routinely used in the detection and mapping of volcanic ash plumes; however, it has collected a significant amount of data from volcanic eruptions [57], including the nascent portion of the plume. Current TIR detection models do not provide information on PSD and AOD in this region, due to the absence of transmitted energy from the surface. However, it is theorized that this opaque region of the plume may behave radiantly as a solid emitting surface [57,58]. If true, pixels in this opaque region can be deconvolved using a linear end-member unmixing model. We use the linear deconvolution model, described by Ramsey and Christensen [38]. This model assumes that each mixed pixel spectrum is created from the sum of the areal percentage of each end-member component. Therefore, if an appropriate end-member library exists, the mixed data can be deconvolved into end-member percentage images. This model can be expressed mathematically for η isothermal end-members as,

$$\varepsilon(\lambda)_{\text{mix}} = \sum_{i=1}^{\eta} \zeta_i \varepsilon(\lambda)_i + \delta(\lambda); \sum_{i=1}^{\eta} \zeta_i = 1.0 \quad (3)$$

where $\varepsilon(\lambda)_{\text{mix}}$ is the mixture spectrum, ζ_i is the areal fraction of the i th end-member ($\varepsilon(\lambda)_i$) and $\delta(\lambda)$ is the residual error. The fit of the library data to that of the satellite data is determined using a root-mean-squared (RMS) error approach. This is determined via the equation,

$$\text{RMS} = \sqrt{\sum_{j=1}^m \delta(\lambda)_j^2 / m} \quad (4)$$

where m is the number of instrument bands. This error is expressed as a value between 0 and 1.0, where lower numbers correspond to a better fit of each model iteration.

To test this hypothesis, the AVAL library was applied using the linear deconvolution model to ASTER TIR image data of a volcanic ash plume emitted from the Sakurajima Volcano, Japan in 2010. Because Sakurajima is one of the ash samples represented in the AVAL library, it is used as the primary end-member suite. The presence of an opaque volcanic ash plume needed to be determined from the image data to proceed with the analysis. To do this (aside from a simple visual determination), temperature transects were taken through the plume-bearing pixels. The plume is considered opaque where the temperature is distinctly lower on the transect. These lower temperatures imply that no ground upwelling radiance has travelled through the plume and been detected by the sensor. Based on these transects, the image was deemed appropriate for analysis with the linear deconvolution model. Figure 5 shows the ASTER image containing a plume generated by the Sakurajima Volcano.

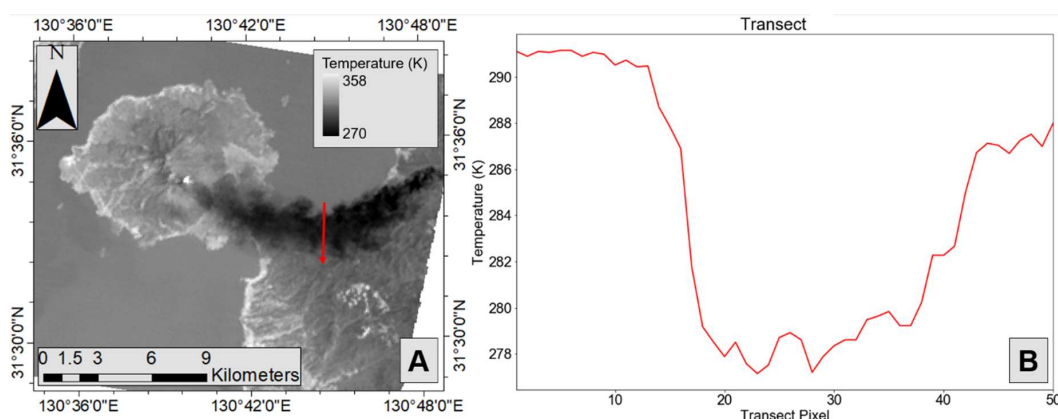


Figure 5. (A) AST_08 temperature product image of the Sakurajima Volcano, captured 29 April 2010. A plume is clearly emanating from the source vent. The red line indicates one of the transects taken through the plume to obtain the temperature information shown in (B). This plot demonstrates the distinct lower temperatures found in the plume relative to the ground surface, as there is a sharp contrast in temperature between these two regions. In this area, it is assumed that the plume is opaque and that ground-upwelling radiance is transmitted through the plume.

The ASTER AST_05 emissivity data product is used as the model input data [59]. This data product is derived from the AST_09T product, which is fully radiometrically and atmospherically calibrated. To derive emissivity, it undergoes further processing in the form of the Temperature Emissivity Separation (TES) algorithm, which has been shown to be accurate to 0.015 emissivity [60,61], making it suitable for use in this study. Preliminary results are shown in Figure 6.

The results using this spectral suite with the linear deconvolution model show dominance of two particle-size fractions. There is also a visible size fraction distribution, with finer particles (dominantly 8–25 μm) found within the core of the ash plume, whereas larger particles (in particular 45–63 μm) are detected in greater abundance at the edges. The other three particle sizes are sparsely represented in the plume; however, they are found present on the flanks of the volcano, most abundantly, the 63–150 and 25–45 particle-size ranges. These first results of plume mapping using a TIR spectral library are interesting. The modeling approach using the Sakurajima AVAL suite produced distinct areal percentages of particle sizes, as well as an RMS error decrease within the plume compared to the land and water surfaces. Furthermore, it is worth noting how 25–45 μm is considered abundant across much of the land and water surface. However, this is where the RMS error map is useful, as these areas are also related to higher RMS errors (>0.5), meaning that there is a poor model fit of the laboratory to image data. The implication is that the Sakurajima AVAL spectra provide the best fit to the plume-bearing pixels, validating the accuracy of the composition and particle-size model distributions. This may be the actual distribution pattern or caused by preferential detection of particles

deeper within the plume's volume due to a more diffuse upper layer at the plume edges. One caveat on the results is the potential effects of ice coating the ash particles. Water vapor is a major constituent of volcanic ash plumes, and ash particles provide a good nucleation site for ice crystallization [62]. This would subsequently change the emissivity spectrum, making the composition and particle size difficult to discern.

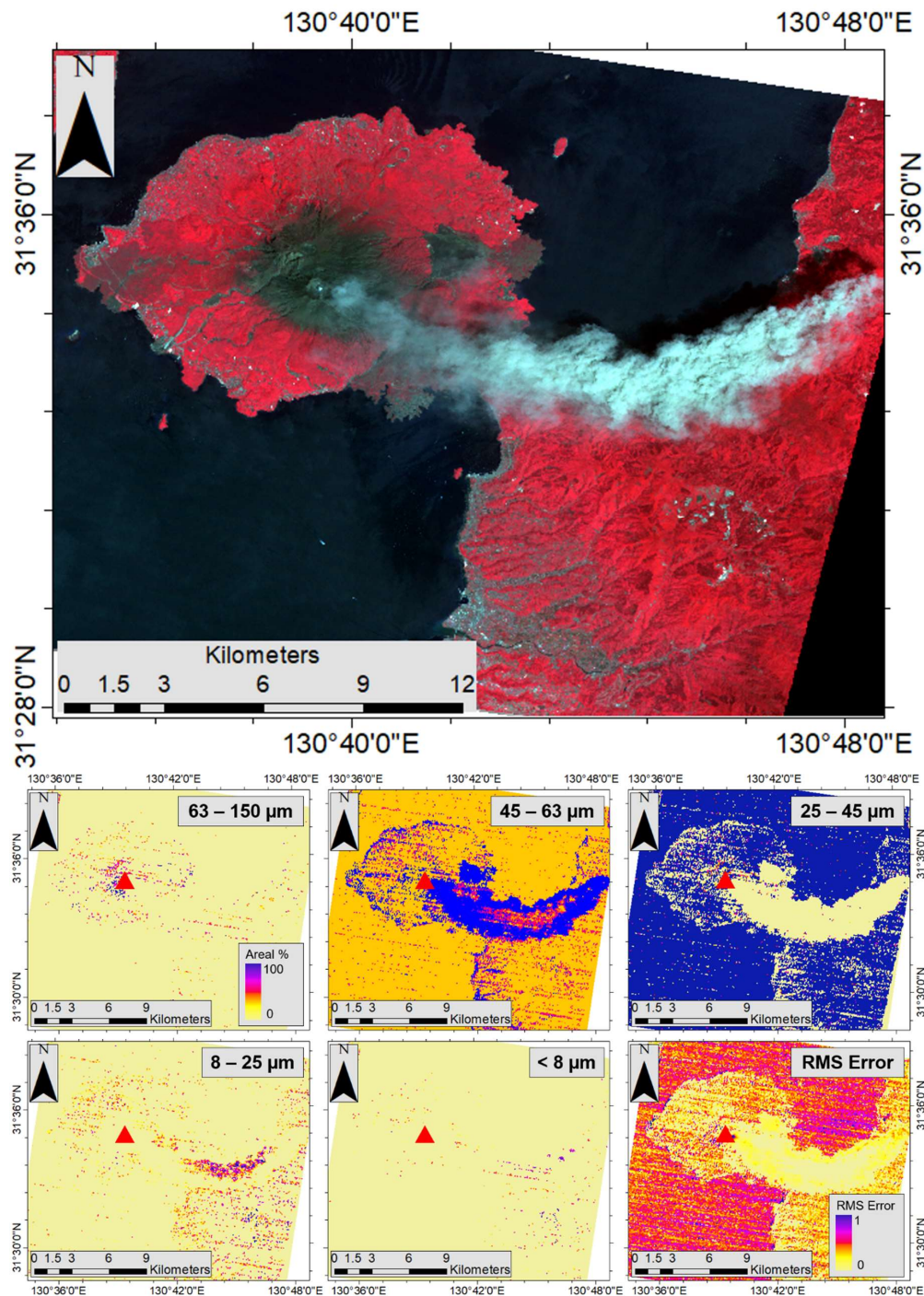


Figure 6. (Top Panel) ASTER VNIR image of the Sakurajima Volcano from 29 April 2010. (Bottom Panels) Areal percentages of each Sakurajima library end-member derived from the linear deconvolution algorithm applied to ASTER data acquired on 29 April 2010. Each panel refers to the particle-size result. The bottom right image is the RMS error (or overall fit of the model). Red triangle indicates the location of the Showa crater from which the ash cloud was generated.

While the primary aim of this study is to observe the properties of opaque volcanic ash clouds, it may also represent an opportunity to map particles of volcanic ash that have been deposited on the flanks of a volcano shortly after eruption. In the example shown in Figure 6, larger particles (those size fractions $>25\ \mu\text{m}$) have provided a good fit for model, and these regions are associated with lower RMS errors. This demonstrates that these libraries could also be used to determine the composition and particle-size range of material deposited on the flanks of a volcano after an eruption has ended. Where a clear ASTER scene does not contain a volcanic ash plume during an eruption, the AVAL library could be used to derive information from deposited material, so that these properties can be mapped.

5. Conclusions

The AVAL library has been created using laboratory TIR emission measurements following painstaking sample preparation and characterization. These samples represent different volcanic environments and conditions, which are reflected in the unique spectral signatures for each sample suite. Furthermore, the use of the MOUDI to separate ash particles $<45\ \mu\text{m}$ into distinct size fractions was successful based on the spectral results. These show the shallowing of the reststrahlen band absorption coupled with development of the longer wavelength transparency feature, each characteristics of decreasing particle size. Applied to ASTER TIR data for the first time, the initial AVAL modeling results for an eruption of the Sakurajima Volcano demonstrate the potential of this approach. With additional testing and further expansion of the AVAL library, multispectral TIR emissivity data of opaque plumes could be deconvolved using a linear deconvolution model to extract the particle-size range, its distribution, and the bulk composition. The implications of this are that this knowledge could be used to better inform transmission-based retrieval models of volcanic ash plumes, by providing them with a more accurate assessment of composition. This will, in turn, lead to better estimations of particle-size distribution and mass from these methods [37]. Furthermore, this method could be used to extract this information from current and future TIR satellite sensors, provided that there are opaque plume-bearing pixels present in the image data. The hyperspectral laboratory measurements will be provided in the IVIS group archive, so that they can be resampled to the spectral resolution of these sensors.

The current AVAL spectral library is the initial phase of a planned larger suite of volcanic ash samples to be used in conjunction with multispectral TIR image data. Library expansion is important and ongoing. It will include additional samples with different wt. % glass versus crystals, as well as samples with different glass compositions. By better understanding how different compositions and particle-size ranges affect the TIR emission spectra, we can better interpret the resulting image-derived data of active volcanic ash plumes, which allows a more detailed volcanological analysis of the ongoing eruption, as well as valuable input data for hazard assessments.

Author Contributions: Conceptualization, D.B.W. and M.S.R.; Formal analysis, D.B.W.; Funding acquisition, D.B.W. and M.S.R.; Investigation, D.B.W. and M.S.R.; Methodology, D.B.W. and M.S.R.; Project administration, M.S.R.; Supervision, M.S.R.; Validation, D.B.W.; Visualization, D.B.W.; Writing—original draft, D.B.W. and M.S.R.; Writing—review & editing, D.B.W. and M.S.R.

Funding: This research was funded by the NASA Science of Terra and Aqua grant (NNX14AQ96G) awarded to MSR, a NASA Earth and Space Science Fellowship (NNX15AQ72H) awarded to DBW, and a National Geographic Committee for Research and Exploration grant awarded to MSR and DBW (9734-15).

Acknowledgments: We would like to thank the reviewers of this manuscript for their feedback which has greatly improved the work presented here. We thank Matthew Watson (U. Bristol), Gustavo Chigna (INSIVUMEH), Masato Iguchi and Daisuke Miki (SVO, U. Kyoto) for their assistance with field logistics in Guatemala and Japan. Furthermore, we thank the Air Quality Laboratory at CMU for use of their facilities, particularly Leif Jahn and Eric Lipsky who assisted with the MOUDI preparation. We would also like to thank Vince Realmuto (NASA JPL) and Stan Mertzman (F&M) for support with and performing the XRF analysis.

Conflicts of Interest: The authors declare no conflict of interest. The funders had no role in the design of the study; in the collection, analyses, or interpretation of data; in the writing of the manuscript, or in the decision to publish the results.

References

1. Heiken, G.; Wohletz, K. *Volcanic Ash*; University Presses of California, Chicago, Harvard & MIT: London, UK, 1985.
2. Rose, W.I.; Durant, A.J. Fine ash content of explosive eruptions. *J. Volcan. Geotherm. Res.* **2009**, *186*, 32–39. [[CrossRef](#)]
3. Heiken, G.; Wohletz, K. Fragmentation processes in explosive volcanic eruptions. In *Sedimentation in Volcanic Settings: SEPM Special Publications*, 1st ed.; Fisher, R.V., Smith, G.A., Eds.; Society for Sedimentary Geology: Tulsa, OK, USA, 1991; Volume 45, pp. 19–26.
4. Klug, C.; Cashman, K.V. Permeability development in vesiculating magmas: implications for fragmentation. *Bull. Volc.* **1996**, *58*, 87–100. [[CrossRef](#)]
5. Brown, R.J.; Bonadonna, C.; Durant, A.J. A review of volcanic ash aggregation. *Phys. Chem. Earth Pts. A/B/C* **2011**, *45–46*, 65–78. [[CrossRef](#)]
6. Brazier, S.; Davis, A.N.; Sigurdsson, H.; Sparks, R.S.J. Fall-out and deposition of volcanic ash during the 1979 explosive eruption of the Soufriere of St. Vincent. *J. Volc. Geotherm. Res.* **1982**, *14*, 335–359. [[CrossRef](#)]
7. Sorem, R.K. Volcanic ash clusters: tephra rafts and scavengers. *J. Volc. Geotherm. Res.* **1982**, *13*, 63–71. [[CrossRef](#)]
8. Parfitt, E.A. A study of clast size distribution, ash deposition and fragmentation in a Hawaiian-style volcanic eruption. *J. Volc. Geotherm. Res.* **1998**, *84*, 197–208. [[CrossRef](#)]
9. Taddeucci, J.; Scarlato, P.; Montanaro, C.; Cimarelli, C.; Del Bello, E.; Freda, C.; Andronico, D.; Gudmundsson, M.T.; Dingwell, D.B. Aggregation-dominated ash settling from the Eyjafjallajökull volcanic cloud illuminated by field and laboratory high-speed imaging. *Geology* **2011**, *39*, 891–894. [[CrossRef](#)]
10. Van Eaton, A.R.; Mastin, L.G.; Herzog, M.; Schwaiger, H.F.; Schneider, D.J.; Wallace, K.L.; Clarke, A.B. Hail formation triggers rapid ash aggregation in volcanic plumes. *Nat. Comms.* **2015**, *6*, 7860. [[CrossRef](#)]
11. Folch, A.; Sulpizio, R. Evaluating long-range volcanic ash hazard using supercomputing facilities: Application to Somma-Vesuvius (Italy), and consequences for civil aviation over the Central Mediterranean Area. *Bull. Volc.* **2010**, *72*, 1039–1059. [[CrossRef](#)]
12. Baxter, P.J.; Bonadonna, C.; Dupree, R.; Hards, V.L.; Kohn, S.C.; Murphy, M.D.; Nichols, A.; Nicholson, R.A.; Norton, G.; Searl, A.; et al. Cristobalite in volcanic ash of the Soufrière Hills volcano, Montserrat, British West Indies. *Science* **1999**, *283*, 1142–1145. [[CrossRef](#)]
13. Horwell, C.J.; Baxter, P.J. The respiratory health hazards of volcanic ash: A review for volcanic risk mitigation. *Bull. Volc.* **2006**, *69*, 1–24. [[CrossRef](#)]
14. Barsotti, S.; Andronico, D.; Nieri, A.; Del Carlo, P.; Baxter, P.J.; Aspinall, W.P.; Hincks, T. Quantitative assessment of volcanic ash hazards for health and infrastructure at Mt. Etna (Italy) by numerical simulation. *J. Volc. Geotherm. Res.* **2010**, *192*, 85–96. [[CrossRef](#)]
15. Bebbington, M.; Cronin, S.J.; Chapman, I.; Turner, M.B. Quantifying volcanic ash fall hazard to electricity infrastructure. *J. Volc. Geotherm. Res.* **2008**, *177*, 1055–1062. [[CrossRef](#)]
16. Cronin, S.J.; Hedley, M.J.; Neal, V.J.; Smith, G. Agronomic impact of tephra fallout from 1995 and 1996 Ruapehu Volcano eruptions, New Zealand. *Env. Geo.* **1998**, *34*, 21–30. [[CrossRef](#)]
17. Guffanti, M.; Tupper, A. Volcanic ash hazards and aviation risk. In *Volcanic Hazards, Risks and Disasters*, 1st ed.; Shroder, J.F., Papale, P., Eds.; Elsevier: New York, NY, USA, 2015; pp. 87–108.
18. Taddeucci, J.; Pompilio, M.; Scarlato, P. Monitoring the explosive activity of the July–August 2001 eruption of Mt. Etna (Italy) by ash characterization. *Geophys. Res. Lett.* **2002**, *29*, 1230. [[CrossRef](#)]
19. Orr, T.R.; Hoblitt, R.P. A Versatile Time-Lapse Camera System Developed by the Hawaiian Volcano Observatory for Use at Kilauea Volcano, Hawaii. Scientific Investigations Report No. 2008–5117; Geological Survey (U.S.): Reston, WA, USA, 2008; pp. 1–8.
20. Pergola, N.; Tramutoli, V.; Marchese, F.; Scaffidi, I.; Lacava, T. Improving volcanic ash cloud detection by a robust satellite technique. *Rem. Sens. Env.* **2004**, *90*, 1–22. [[CrossRef](#)]
21. Folch, A.; Costa, A.; Macedonio, G. FALL3D: A computational model for transport and deposition of volcanic ash. *Comp. Geosci.* **2009**, *35*, 1334–1342. [[CrossRef](#)]
22. Realmuto, V.J.; Worden, H.M. Impact of atmospheric water vapor on the thermal infrared remote sensing of volcanic sulfur dioxide emissions: A case study from the Pu‘u ‘O‘vent of Kilauea Volcano, Hawaii. *J. Geophys. Res. Sol. Earth.* **2000**, *105*, 21497–21507. [[CrossRef](#)]

23. Urai, M. Sulfur dioxide flux estimation from volcanoes using advanced spaceborne thermal emission and reflection radiometer—a case study of Miyakejima volcano, Japan. *J. Volc. Geotherm. Res.* **2004**, *134*, 1–13. [[CrossRef](#)]
24. Prata, A.J. Observations of volcanic ash clouds in the 10–12 μm window using AVHRR/2 data. *Int. J. Rem. Sens.* **1989**, *10*, 751–761. [[CrossRef](#)]
25. Prata, A.J. Infrared radiative transfer calculations for volcanic ash clouds. *Geophys. Res. Lett.* **1989**, *16*, 1293–1296. [[CrossRef](#)]
26. Elrod, G.P.; Connell, B.H.; Hillger, D.W. Improved detection of airborne volcanic ash using multispectral thermal infrared satellite data. *J. Geophys. Res. Atmos.* **2003**, *108*. [[CrossRef](#)]
27. Pavolonis, M.J.; Feltz, W.F.; Heidinger, A.K.; Gallina, G.M. A daytime complement to the reverse absorption technique for improved automated detection of volcanic ash. *J. Atmos. Ocean. Tech.* **2006**, *23*, 1422–1444. [[CrossRef](#)]
28. Webley, P.W.; Lopez, T.M.; Ekstrand, A.L.; Dean, K.G.; Rinkleff, P.; Dehn, J.; Cahill, C.F.; Wessels, R.L.; Bailey, J.E.; Izbekov, P.; et al. Remote observations of eruptive clouds and surface thermal activity during the 2009 eruption of Redoubt volcano. *J. Volc. Geotherm. Res.* **2013**, *259*, 185–200. [[CrossRef](#)]
29. Pavolonis, M.J.; Sieglaff, J.; Cintineo, J. Automated Detection of Explosive Volcanic Eruptions Using Satellite-Derived Cloud Vertical Growth Rates. *Earth Space Sci.* **2018**, *5*, 903–928. [[CrossRef](#)]
30. Wen, S.; Rose, W.I. Retrieval of sizes and total masses of particles in volcanic clouds using AVHRR bands 4 and 5. *J. Geophys. Res. Atmos.* **1994**, *99*, 5421–5431. [[CrossRef](#)]
31. Prata, A.J.; Grant, I.F. Retrieval of microphysical and morphological properties of volcanic ash plumes from satellite data: Application to Mt Ruapehu, New Zealand. *Quart. J. Royal Meteor. Soc.* **2001**, *127*, 2153–2179. [[CrossRef](#)]
32. Simpson, J.J.; Hufford, G.; Pieri, D.; Berg, J. Failures in detecting volcanic ash from a satellite-based technique. *Rem. Sens. Environ.* **2000**, *72*, 191–217. [[CrossRef](#)]
33. Prata, F.; Bluth, G.; Rose, B.; Schneider, D.; Tupper, A. Comments on “Failures in detecting volcanic ash from a satellite-based technique”. *Rem. Sens. Environ.* **2001**, *78*, 341–346. [[CrossRef](#)]
34. Bonadonna, C.; Folch, A.; Loughlin, S.; Puempel, H. Future developments in modelling and monitoring of volcanic ash clouds: Outcomes from the first IAVCEI-WMO workshop on Ash Dispersal Forecast and Civil Aviation. *Bull. Volc.* **2012**, *74*, 1–10. [[CrossRef](#)]
35. Pollack, J.B.; Toon, O.B.; Khare, B.N. Optical properties of some terrestrial rocks and glasses. *Icarus* **1973**, *19*, 372–389. [[CrossRef](#)]
36. Reed, B.E.; Peters, D.M.; McPheat, R.; Grainger, R.G. The complex refractive index of volcanic ash aerosol retrieved from spectral mass extinction. *J. Geophys. Res. Atmos.* **2018**, *123*, 1339–1350. [[CrossRef](#)]
37. Mackie, S.; Millington, S.; Watson, I.M. How assumed composition affects the interpretation of satellite observations of volcanic ash. *Meteor. App.* **2014**, *21*, 20–29. [[CrossRef](#)]
38. Ramsey, M.S.; Christensen, P.R. Mineral abundance determination: Quantitative deconvolution of thermal emission spectra. *J. Geophys. Res. Sol. Earth* **1998**, *103*, 577–596. [[CrossRef](#)]
39. Walter, L.S.; Salisbury, J.W. Spectral characterization of igneous rocks in the 8-to 12- μm region. *J. Geophys. Res. Sol. Earth.* **1989**, *94*, 9203–9213. [[CrossRef](#)]
40. Rowan, L.C.; Salisbury, J.W.; Kingston, M.J.; Vergo, N.; Bostick, N.H. Evaluation of visible and near-infrared and thermal-infrared reflectance spectra for studying thermal alteration of Pierre Shale, Wolcott, Colorado. *J. Geophys. Res. Sol. Earth.* **1991**, *96*, 18047–18057. [[CrossRef](#)]
41. Clark, R.N.; Swayze, G.A.; Wise, R.; Livo, E.; Hoefen, T.; Kokaly, R.; Sutley, S.J. USGS digital spectral library splib06a: U.S. Geological Survey, Digital Data Series 231. 2006. Available online: <http://speclab.cr.usgs.gov/spectral.lib06> (accessed on 17 November 2018).
42. Baldridge, A.M.; Hook, S.J.; Grove, C.I.; Rivera, G. The ASTER Spectral library version 2.0. *Rem. Sens. Environ.* **2009**, *113*, 711–715. [[CrossRef](#)]
43. Christensen, P.R.; Bandfield, J.L.; Hamilton, V.E.; Howard, D.A.; Lane, M.D.; Piatek, J.L.; Ruff, S.W.; Stefanov, W.L. A thermal emission spectral library of rock-forming minerals. *J. Geophys. Res.* **2000**, *105*, 9735–9739. [[CrossRef](#)]
44. Horwell, C.J. Grain-size analysis of volcanic ash for the rapid assessment of respiratory health hazard. *J. Environ. Monitor.* **2007**, *9*, 1107–1115. [[CrossRef](#)]

45. Cashman, K.V.; Rust, A.C. (2015) Volcanic Ash: Generation and Spatial Variations. In *Volcanic Ash: Hazard Observation*, 1st ed.; Mackie, S., Cashman, K.V., Ricketts, H., Rust, A.C., Watson, I.M., Eds.; Elsevier: Amsterdam, The Netherlands, 2015; pp. 5–22.
46. Byrnes, J.M.; Ramsey, M.S.; King, P.L.; Lee, R.J. Thermal infrared reflectance and emission spectroscopy of quartzofeldspathic glasses. *Geophys. Res. Lett.* **2007**, *34*, L01306. [[CrossRef](#)]
47. King, P.L.; McMillan, P.F.; Moore, G.M. Infrared spectroscopy of silicate glasses with application to natural systems. In *Infrared Spectroscopy in Geochemistry, Exploration Geochemistry and Remote Sensing*, 1st ed.; King, P.L., Ramsey, M.S., Swayze, G.A., Eds.; Mineralogical Association of Canada: London, Ontario, 2004; pp. 93–133.
48. Minitti, M.E.; Hamilton, V.E. A search for basaltic-to-intermediate glasses on Mars: Assessing Martian crustal mineralogy. *Icarus* **2010**, *210*, 135–149. [[CrossRef](#)]
49. Salisbury, J.W.; Wald, A. The role of volume scattering in reducing spectral contrast of reststrahlen bands in spectra of powdered minerals. *Icarus* **1992**, *96*, 121–128. [[CrossRef](#)]
50. Marple, V.A.; Rubow, K.L.; Behm, S.M. A microorifice uniform deposit impactor (MOUDI): Description, calibration, and use. *Aero. Sci. Tech.* **1991**, *14*, 434–446. [[CrossRef](#)]
51. Ruff, S.W.; Christensen, P.R.; Barbera, P.W.; Anderson, D.L. Quantitative thermal emission spectroscopy of minerals: A laboratory technique for measurement and calibration. *J. Geophys. Res. Sol. Earth.* **1997**, *102*, 14899–14913. [[CrossRef](#)]
52. Abbey, S. Studies In “standard samples” of silicate rocks and minerals 1969–1982. *Can. Geol. Surv. Paper* **1983**, *114*, 83–15.
53. Govindaraju, K. 1994 compilation of working values and sample description for 383 geostandards. *Geostandards News* **1994**, *18*, 1–158. [[CrossRef](#)]
54. Logan, L.M.; Hunt, G.R.; Salisbury, J.W.; Balsamo, S.R. Compositional implications of Christiansen frequency maximums for infrared remote sensing applications. *J. Geophys. Res.* **1973**, *78*, 4983–5003. [[CrossRef](#)]
55. Conel, J.E. Infrared emissivities of silicates: Experimental results and a cloudy atmosphere model of spectral emission from condensed particulate mediums. *J. Geophys. Res.* **1996**, *74*, 1614–1634. [[CrossRef](#)]
56. Ramsey, M.S.; Fink, J.H. Estimating silicic lava vesicularity with thermal remote sensing: A new technique for volcanic mapping and monitoring. *Bull. Volc.* **1999**, *61*, 32–39. [[CrossRef](#)]
57. Ramsey, M.S. Synergistic use of satellite thermal detection and science: A decadal perspective using ASTER. *Geo. Soc. Lond. Spec. Pub.* **2016**, *426*, 115–136. [[CrossRef](#)]
58. Williams, D.B. An analysis of proximal volcanic ash emissions. Doctoral Dissertation, University of Pittsburgh, Pittsburgh, PA, USA, 11 August 2018.
59. Abrams, M. The Advanced Spaceborne Thermal Emission and Reflection Radiometer (ASTER): Data products for the high spatial resolution imager on NASA’s Terra platform. *Int. J. of Rem. Sens.* **2000**, *21*, 847–859. [[CrossRef](#)]
60. Gillespie, A.; Rokugawa, S.; Matsunaga, T.; Cothorn, J.S.; Hook, S.; Kahle, A.B. A temperature and emissivity separation algorithm for Advanced Spaceborne Thermal Emission and Reflection Radiometer (ASTER) images. *IEEE Trans. Geo. Rem. Sens.* **1998**, *36*, 1113–1126. [[CrossRef](#)]
61. Gustafson, W.T.; Gillespie, A.R.; Yamada, G.J. Revisions to the ASTER temperature/emissivity separation algorithm. In Proceedings of the 2nd International Symposium on Recent Advances in Quantitative Remote Sensing, University of Valencia Global Change Unit, Torrent, Spain, 25–29 September 2006.
62. Kulkarni, G.; Nandasiri, M.; Zelenyuk, A.; Beranek, J.; Madaan, N.; Devaraj, A.; Shutthanandan, V.; Thevuthasan, S.; Varga, T. Effects of crystallographic properties on the ice nucleation properties of volcanic ash particles. *Geophys. Res. Lett.* **2015**, *42*, 3048–3055. [[CrossRef](#)]

